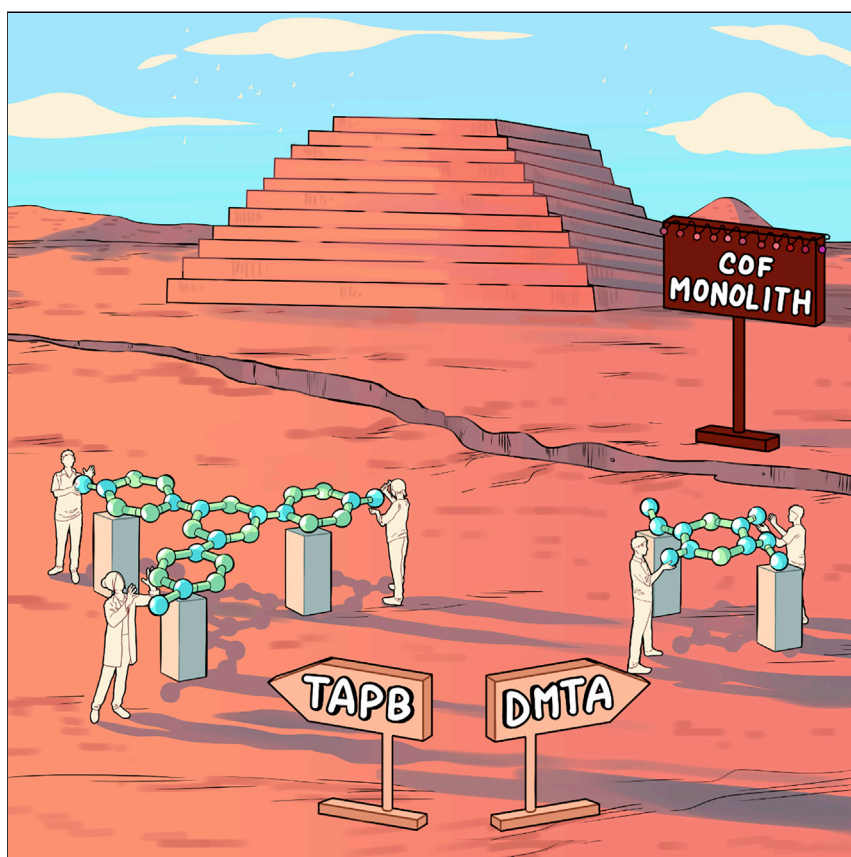


## Article

# Sol-gel processing of a covalent organic framework for the generation of hierarchically porous monolithic adsorbents



Industrial application of porous materials frequently requires shaping into pellets. However, emerging porous materials are often incompatible with existing methods of pelletization as a result of their limited mechanical stability. Here, we present a simple way to prepare hierarchically porous centimeter-scale covalent organic framework (COF) monoliths. Monoliths thus formed exhibit gas-uptake capacities above those of powder or single-crystal analogs of the same material and afford improved separation performance relative to that of powder controls for industrially relevant separations.

Mark E. Carrington, Nakul Rampal, David G. Madden, ..., Sergei Taraskin, Karena W. Chapman, David Fairen-Jimenez

df334@cam.ac.uk

## Highlights

COFs are shown to be frequently unstable to in-plane mechanical shear

A method of COF monolith formation that enables hierarchical porosity is presented

Hierarchical mesopores enable improved gas uptake and selectivity

Hierarchical porosity can be accurately modeled via lattice-gas methods



Carrington et al., Chem 8, 1–17  
November 10, 2022 © 2022 The Author(s).  
Published by Elsevier Inc.  
<https://doi.org/10.1016/j.chempr.2022.07.013>

Article

# Sol-gel processing of a covalent organic framework for the generation of hierarchically porous monolithic adsorbents

Mark E. Carrington,<sup>1,10</sup> Nakul Rampal,<sup>1,10</sup> David G. Madden,<sup>1</sup> Daniel O’Nolan,<sup>2</sup> Nicola Pietro Maria Casati,<sup>3</sup> Giorgio Divitini,<sup>4</sup> Jesús Á. Martín-Illán,<sup>5</sup> Michele Tricarico,<sup>6</sup> Ritums Cepitis,<sup>7</sup> Ceren Çamur,<sup>1</sup> Teresa Curtin,<sup>8</sup> Joaquin Silvestre-Albero,<sup>9</sup> Jin-Chong Tan,<sup>6</sup> Felix Zamora,<sup>5</sup> Sergei Taraskin,<sup>7</sup> Karena W. Chapman,<sup>2</sup> and David Fairen-Jimenez<sup>1,11,\*</sup>

## SUMMARY

Covalent organic frameworks (COFs) have emerged as a versatile material platform for such applications as chemical separations, chemical reaction engineering, and energy storage. Their inherently low mechanical stability, however, frequently renders existing methods of pelletization ineffective, contributing to pore collapse, pore blockage, or insufficient densification of crystallites. Here, we present a process for the shaping and densifying of COFs into robust centimeter-scale porous monoliths without the need for templates, additives, or binders. This process minimizes mechanical damage from shear-induced plastic deformation and further provides a network of interparticle mesopores that we exploit in accessing analyte capacities above those achievable from the intrinsic COF structure. Using a lattice-gas model, we accurately capture the monolithic structure across the mesoporous range and tie pore architecture to performance in both gas-storage and -separation applications. Collectively, these results represent a substantial step in the practical applicability of COFs and other mechanically weak porous materials.

## INTRODUCTION

Porous materials capable of reducing both the cost and energy intensity of industrial chemical processes are critically needed in transitioning to a carbon-neutral energy cycle.<sup>1,2</sup> Constructed from Earth-abundant elements and affording a combination of chemo-structural diversity, ease of synthetic modification, and relative chemical stability, covalent organic frameworks (COFs) have emerged as attractive alternatives to existing porous materials, including activated carbons, zeolites, and metal-organic frameworks (MOFs).<sup>3–5</sup> However, a technological limit has been reached where traditional methods of adsorbent post-processing are poorly suited to COFs as a result of the low mechanical stability frequently exhibited by these materials.<sup>6–11</sup> To date, these mechanical characteristics have been shown to limit the pressures that can be used during pelletization<sup>6,12</sup> and the selection of fluids available for activation,<sup>8–10</sup> deviations from which can result in sharp losses in capacity. Although factors such as framework topology and linker length can be synthetically tuned to target more robust architectures,<sup>13</sup> the inverse approach—i.e., whereby a desired COF can be shaped into an industrially relevant form factor without compromising key performance metrics—has not been attempted.

## THE BIGGER PICTURE

Porous materials are frequently used industrially as macroscopic pellets exhibiting interstitial space porosity. Although conventional methods of pelletization are suitable for mechanically robust materials, similar processing methods result in sharp losses in capacity in state-of-the-art adsorbent materials as a result of their inherently lower degrees of mechanical stability. Here, we show that COFs synthesized to date are frequently unstable to in-plane mechanical shear and further present a simple, rapid, and general process for the preparation of centimeter-scale, hierarchically porous, monolithic COFs. COF monoliths thus prepared exhibit a system of intercrystallite mesopores, which push final gas-uptake capacities to levels above those for powder or single-crystal analogs of the same material. These characteristics, without any chemical modification, enable both improved uptake capacity and mixed-gas selectivity for target gases within industrially relevant gaseous compositions.

Here, we report a simple and rapid process for the shaping of COFs into macroscopic pellets without the use of binders, templates, or additives and without any further processing steps needed for a final application. For an archetypical two-dimensional (2D) COF, TPB-DMTP-COF,<sup>14</sup> we demonstrate control over the degree of aggregation of crystallites within pellets and systematically identify the presence of a lower limit in intercrystallite pore size for a given activation solvent. We tie this limit to the onset of capillary-action-induced, turbostratic disordering of crystallites and further confirm that mechanical damage can be avoided through the use of an activation fluid with an ultra-low surface tension. COF monoliths thus prepared are mechanically robust and exhibit low-pressure adsorption characteristics identical to those of the best-reported powder analogs. They additionally benefit from a system of interparticle mesopores that push final adsorption capacities above levels expected for single crystals. We capture these structural characteristics in a lattice-gas model, which accurately reproduces experimentally derived isotherms for COF monoliths *in silico*. The combination of intact crystallites, mechanical robustness, high bulk densities, and regular hierarchical mesopores is unique among COF monoliths demonstrated to date. These properties result in industrially suitable monoliths that afford better gas-adsorption performance characteristics for both pure-component gas storage (CO<sub>2</sub> and CH<sub>4</sub>) and mixed-gas chemical separation (CO<sub>2</sub>/N<sub>2</sub> and CO<sub>2</sub>/CH<sub>4</sub>) applications than do unprocessed powder controls. On the basis of these findings, our work provides not only a path forward for the industrial applicability of COFs but also a systematic framework through which COF microstructure and final adsorption properties can be tuned without altering the underlying COF chemistry.

## RESULTS AND DISCUSSION

### High-throughput calculation of mechanical properties

2D COFs are thought to be unstable to in-plane mechanical shear.<sup>11</sup> To evaluate the mechanical properties of COFs across topologies and linkage chemistries, we first performed a high-throughput screen of all reported COFs as inventoried in the CURATED (Clean, Uniform, Refined with Automatic Tracking from Experimental Database) COF database<sup>15</sup> and compared their bulk moduli, shear moduli, and elastic constants with those of MOFs<sup>13</sup> (Figure 1). Within a largest cavity diameter (LCD) range of 15–40 Å, the bulk and shear moduli of COFs were found to be similar to those of MOFs, although COFs exhibited marginally higher bulk moduli and shear moduli on average. However, at lower LCD ranges characteristic of ultramicroporous (<7 Å) and microporous (<20 Å) materials, the bulk and shear moduli of COFs were found to be substantially lower than those of MOFs, suggesting an inherently greater tendency of COFs to mechanically deform even in the absence of larger (>15 Å) pores. To gain insights into the mechanical stability of these materials, we then analyzed the elastic constants ( $c_{ij}$ ) of a representative COF subset, hexagonal 2D COFs, which currently account for 54% of 2D COFs and 45% of all COFs synthesized to date. Applying the stability criteria,  $c_{11} > |c_{12}|$ ,  $c_{33}(c_{11} + 2c_{12}) > 2(c_{13})^2$ ,  $c_{11}c_{33} > (c_{13})^2$  and  $c_{44} > 0$ , we found a majority (64%) of hexagonal 2D COFs to be unstable, confirming weakness to mechanical shear as a predominating feature of these materials and possibly shedding light on the low degrees of crystallinity frequently exhibited by these materials. Given that conventional methods of powder pelletization routinely employ pressures in the range of 1–3 GPa, which are known to trigger losses in capacity within MOFs,<sup>16–21</sup> we sought a revised approach for COF processing and pelletization.

### Sol-gel processing of COFs

To permit ease of experimental benchmarking and analysis, we identified TPB-DMTP-COF as a representative 2D COF with an LCD of 25 Å and excellent known

<sup>1</sup>Adsorption & Advanced Materials Laboratory (AAML), Department of Chemical Engineering & Biotechnology, University of Cambridge, Philippa Fawcett Drive, Cambridge CB3 0AS, UK

<sup>2</sup>Department of Chemistry, Stony Brook University, 100 Nicolls Road, Stony Brook, NY 11794, USA

<sup>3</sup>Laboratory for Synchrotron Radiation—Condensed Matter, Paul Scherrer Institute, 5232 Villigen-PSI, Switzerland

<sup>4</sup>Electron Microscopy Group, Department of Materials Science and Metallurgy, University of Cambridge, 27 Charles Babbage Road, Cambridge CB3 0FS, UK

<sup>5</sup>Departamento de Química Inorgánica, Universidad Autónoma de Madrid, 28049 Madrid, Spain

<sup>6</sup>Multifunctional Materials & Composites (MMC) Laboratory, Department of Engineering Science, University of Oxford, Parks Road, Oxford OX1 3PJ, UK

<sup>7</sup>Department of Chemistry, University of Cambridge, Lensfield Road, Cambridge CB2 1EW, UK

<sup>8</sup>Bernal Institute, Department of Chemical Sciences, University of Limerick, Limerick V94 T9PX, Republic of Ireland

<sup>9</sup>Laboratorio de Materiales Avanzados, Departamento de Química Inorgánica-Instituto Universitario de Materiales, Universidad de Alicante, 03690 San Vicente del Raspeig, Spain

<sup>10</sup>These authors contributed equally

<sup>11</sup>Lead contact

\*Correspondence: [df334@cam.ac.uk](mailto:df334@cam.ac.uk)  
<https://doi.org/10.1016/j.chempr.2022.07.013>

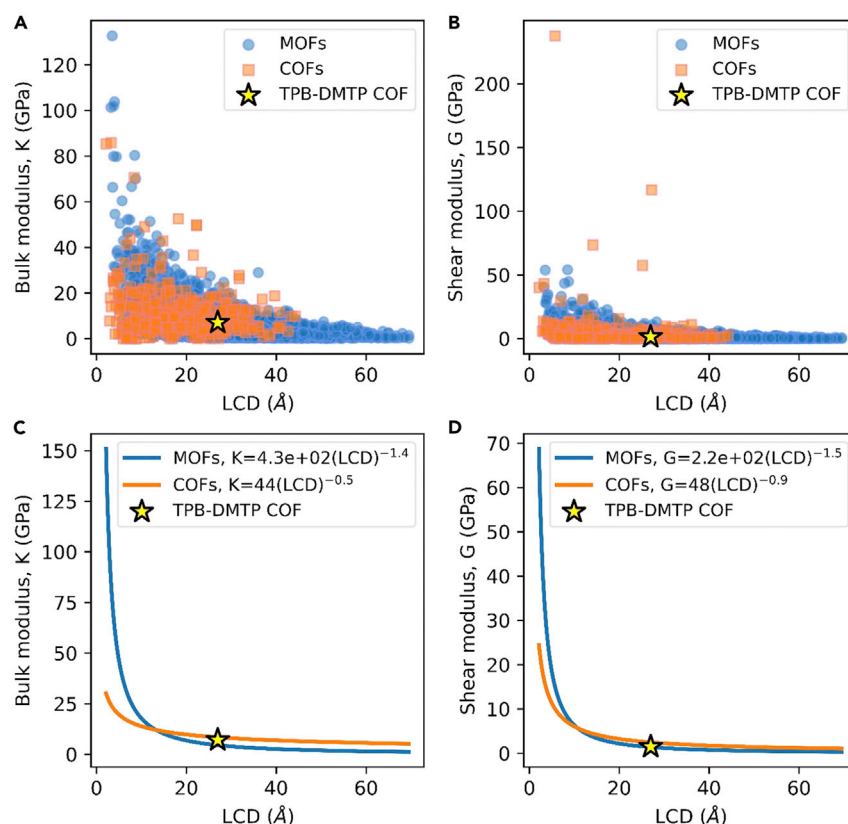


**Figure 1. Calculation of mechanical properties**

(A) Relationship between bulk modulus, K (GPa), and LCD (Å).

(B) Relationship between shear modulus, G (GPa), and LCD (Å).

(C) Exponential fits to the data shown in (A).

(D) Exponential fits to the data shown in (B).

MOFs are in blue, COFs are in orange, and TPB-DMTP-COF is the yellow star.

crystallinity. Upon screening a variety of synthesis solvent systems, we identified acetonitrile and a 1:1 (v/v) mixture of 1,3,5-trimethylbenzene (mesitylene) and 1,4-dioxane (dioxane) as two systems capable of both solubilizing the starting materials and producing crystalline samples of TPB-DMTP-COF. However, whereas the 1:1 (v/v) mixture of mesitylene and dioxane produced powder samples consisting of aggregated particles > 500 nm in diameter (Figures 2E and S5A), the acetonitrile system produced dense pellets consistent with those previously described for MOF monoliths and composed of particles of approximately 40 nm in diameter (Figures 2E and S5H)—well within the limits previously established for monolith formation in MOFs<sup>17,18</sup> (i.e., <120 nm). Taking these two systems as extremes, we used solvent compositions consisting of different fractions of each to prepare pellets as follows: (1) reaction for a fixed amount of time (typically 30 min), (2) centrifugation, (3) purification and solvent exchange to methanol, and (4) controlled drying and activation (Figure 2).

Upon processing, scanning electron microscopy (SEM) of the finished pellets revealed a gradual progression in microstructure from larger, loosely aggregated particles to densely packed monoliths exhibiting conchoidal fracture and little to no interparticle free volume (Figures 2E and S5). Analysis of the nitrogen adsorption isotherms (Figures 3A and S3) collected for these pellets, however, revealed a striking



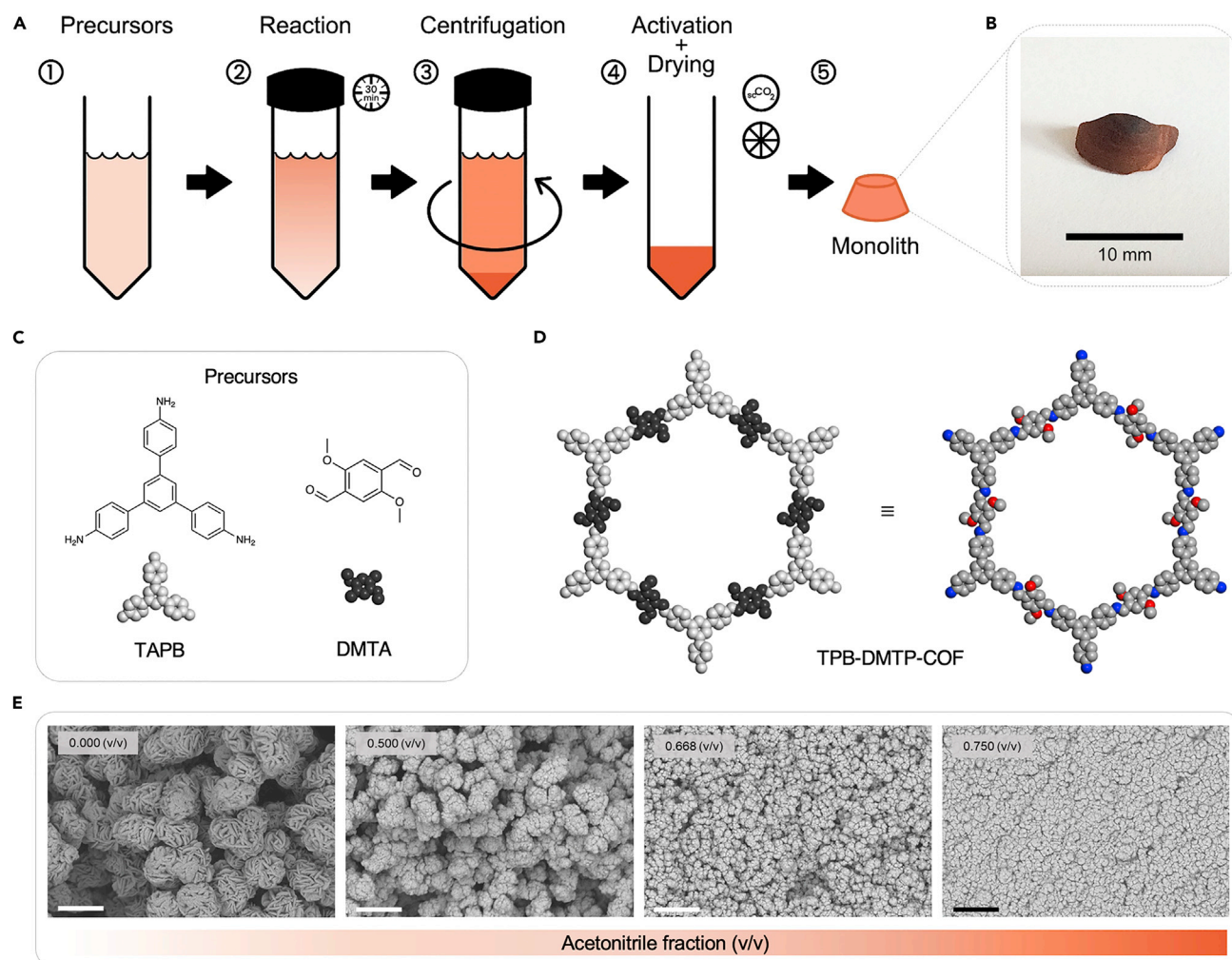


**Figure 2. TPB-DMTP-COF monolith synthesis and structure**

(A) Processing workflow for TPB-DMTP-COF monolith formation.

(B) TPB-DMTP-COF monolith.

(C) Organic precursors used in the synthesis of the COF monolith. TAPB, 1,3,5-tris(4-aminophenyl)benzene (gray); DMTA, 2,5-dimethoxybenzene-1,4-dicarboxaldehyde (black).

(D) Pore structure of TPB-DMTP-COF shows the arrangement of building blocks (left) and elements (right). C atoms are in gray, N atoms are in blue, and O atoms are in red; H atoms have been omitted for clarity.

(E) SEM images of the TPB-DMTP-COF monolith synthesized with varying acetonitrile fractions (left to right): 0.000 (v/v), 0.500 (v/v), 0.688 (v/v), and 0.750 (v/v). Scale bars represent 1  $\mu\text{m}$ .

trend. Whereas we observed a monotonic increase in Brunauer-Emmett-Teller (BET) area—calculated by BET surface identification (BETSI)<sup>22</sup>—for pellets synthesized in solvent systems containing acetonitrile fractions ranging from 0.000 to 0.750 (v/v), we observed a sharp decrease in BET area to  $4 \text{ m}^2 \text{ g}^{-1}$  for samples prepared at higher acetonitrile fractions (Figure 3C). As a result, the highest BET area that could be obtained for TPB-DMTP-COF with methanol as the activation solvent was  $1,122 \text{ m}^2 \text{ g}^{-1}$ , suggesting the presence of a lower limit in intercrystallite pore size beyond which pore disruption takes place. To test whether this pore disruption was being induced by capillary action,<sup>10</sup> we prepared a further sample in a pure acetonitrile solvent system and processed it as before but this time dried and activated it in supercritical carbon dioxide ( $\text{scCO}_2$ ) instead of in methanol and air. The finished pellet not only recovered full porosity but also lay on the monotonic trend previously described

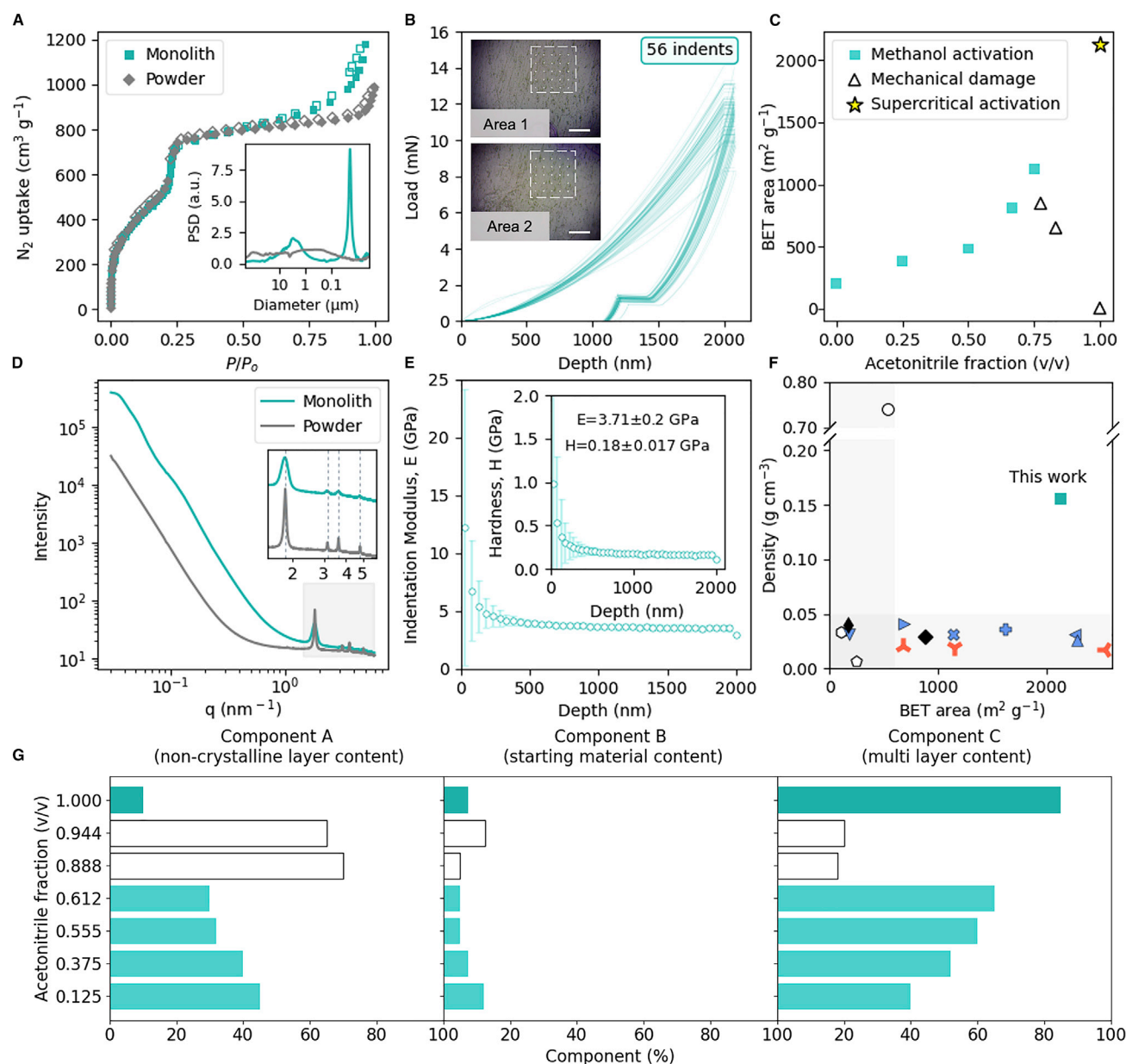


**Figure 3. Structural characterization of TPB-DMTP-COF monoliths**

(A)  $N_2$  adsorption isotherms at 77 K for the 3 bar  $\text{h}^{-1}$   $\text{scCO}_2$ -activated 1.000 (v/v) TPB-DMTP-COF monolith (turquoise squares) and powder (gray diamonds); the inset shows the respective mercury pore-size distributions (PSDs) of the 3 bar  $\text{h}^{-1}$   $\text{scCO}_2$ -activated 1.000 (v/v) TPB-DMTP-COF monolith (turquoise) and powder (gray).

(B) Indentation load versus penetration depth for 56 indents in the 3 bar  $\text{h}^{-1}$   $\text{scCO}_2$ -activated 1.000 (v/v) TPB-DMTP-COF monolith; insets are optical micrographs showing the array of residual indents taken in different areas of the 3 bar  $\text{h}^{-1}$   $\text{scCO}_2$ -activated 1.000 (v/v) TPB-DMTP-COF monolith. Scale bars represent 100  $\mu\text{m}$ .

(C) BET area versus acetonitrile fraction (v/v) of methanol-activated samples (turquoise squares), samples with mechanical damage (white triangles), and supercritically activated (3 bar  $\text{h}^{-1}$ ) sample (yellow star).

(D) SAXS data of the supercritically activated (3 bar  $\text{h}^{-1}$ ) TPB-DMTP COF monolith (turquoise) and powder (gray). The inset shows the characteristic Bragg peaks in the WAXS region; the monolith curve has been offset along the y axis for clarity.

(E) Indentation modulus and hardness (inset) versus penetration depth averaged over 56 indents. Error bars represent standard deviations calculated from 56 measurements made for the 3 bar  $\text{h}^{-1}$   $\text{scCO}_2$ -activated 1.000 (v/v) TPB-DMTP-COF monolith.

(F) Comparison of density ( $\text{g cm}^{-3}$ ) and BET area ( $\text{m}^2 \text{g}^{-1}$ ) values for different COF aerogels, monoliths, and pellets synthesized in the literature. Filled symbols are for COF aerogels, monoliths, and pellets synthesized without the use of any binders, additives, or high pressure: ■, 3 bar  $\text{h}^{-1}$   $\text{scCO}_2$ -activated 1.000 (v/v) TPB-DMTP-COF monolith (this work); ◆, TFPT-HZ-COF;<sup>24</sup> ◆, TPT-HZ-COF;<sup>24</sup> ▼, TAPA-TFPA;<sup>25</sup> ▲, TAPB-PDA;<sup>25</sup>

**Figure 3. Continued**

◀ TAPB-OMePDA;<sup>25</sup> ▶, TAPB-BrPDA;<sup>25</sup> ⊕, TAPB-TFPA;<sup>25</sup> ⊗, BPDA-BTCA;<sup>25</sup> ♡, TAPB-BTCA-AGCOF;<sup>26</sup> ▲, PPDA-BTCA-AGCOF;<sup>26</sup> and ◀, TAPB-PDA-AGCOF.<sup>26</sup> Unfilled symbols are for COF aerogels, monoliths, and pellets synthesized with the use of binders, additives, or high pressure: ○, M<sub>BTCA</sub>;<sup>27</sup> ◻, COF/rGO;<sup>28</sup> and ◯, COF-IL@chitosan.<sup>29</sup>

(G) PDF-XRD bar chart showing the percentages of component A (non-crystalline-layer content), component B (starting-material content), and component C (multilayer content) as a function of acetonitrile fraction (v/v) for each sample studied.

in that it exhibited a BET area of 2,125 m<sup>2</sup> g<sup>-1</sup>—slightly above those previously described for powder analogs of TPB-DMTP-COF.<sup>14</sup> When a higher rate of scCO<sub>2</sub> pressure release (8 versus 3 bar h<sup>-1</sup>) was used during the activation of an identically prepared 1.000 acetonitrile pellet, a reduction in BET area to 1,439 m<sup>2</sup> g<sup>-1</sup> was observed, further suggesting that losses in BET area occur as a result of damage induced by capillary action. Collectively, these results suggest that intercrystallite pore size is modulated during synthesis by control over particle size—where interparticle pores are the void space created by the fundamentally imperfect packing of approximate hard spheres.<sup>23</sup> Where characteristic interparticle pore size falls below a certain threshold, capillary action during drying causes damage to crystallites.

To gain deeper insights into the structural changes accompanying these bulk characteristics, we used a combination of pair distribution function (PDF) and X-ray diffraction (XRD) (supplemental information section S6). Non-negative matrix factorization of the PDF-XRD data revealed three independent underlying components that we attribute to non-crystalline-layer COF content, residual starting-material content, and multilayer (i.e., crystalline) COF content: components A, B, and C, respectively (Figure 3G). For methanol-activated pellets below an acetonitrile fraction of 0.75, a respective decrease and increase in components A and C were observed as the acetonitrile fraction was increased, indicating that TPB-DMTP-COF crystallinity gradually improves before the onset of mechanical damage. Above an acetonitrile fraction of 0.750 (v/v), crystallinity sharply declines, resulting in an increased content of non-crystalline-layer TPB-DMTP-COF, as seen from the increasing weighting of component A. When scCO<sub>2</sub> is used during drying and activation, the multilayer content is recovered—an observation consistent with findings from nitrogen adsorption studies and providing clear evidence for a correlation between mechanical disruption of COF crystallites during post-processing and observable gas-uptake capacities as previously noted for powdered COF systems.<sup>8</sup>

To better understand the mechanism of crystallite disordering into non-crystalline layers within COF monoliths, we performed a combination of high-resolution transmission electron microscopy (HR-TEM) and NanoBlitz indentation studies on a methanol-activated 1.000 acetonitrile control sample for which crystallites are sufficiently disrupted to afford a BET area of 4 m<sup>2</sup> g<sup>-1</sup> (Figure 4). Analysis of the microstructure both within the bulk and within a few layers of the monolith indicated a series of small multilayer crystalline domains bridged by less-ordered regions. Fourier transforms of the image (Figure 4C, inset) further revealed that these features result in a single diffuse band corresponding to a real-space length of 0.36 nm—consistent with interlayer spacing values obtained from analysis of components A (0.37 nm) and C (0.35 nm) derived from the PDF-XRD data. These results suggest that a crystalline-to-turbostratic-disordering mechanism, similar to that observed in mechanically milled graphite, might be responsible for losses in observed porosity within monoliths. At the macroscopic level, NanoBlitz indentation mapping revealed heterogeneities in both the indentation modulus and the mechanical hardness across a 200 × 200 μm region of the material. Given that turbostratic disordering is triggered by capillary action, differences in the local structure of the monolith during drying



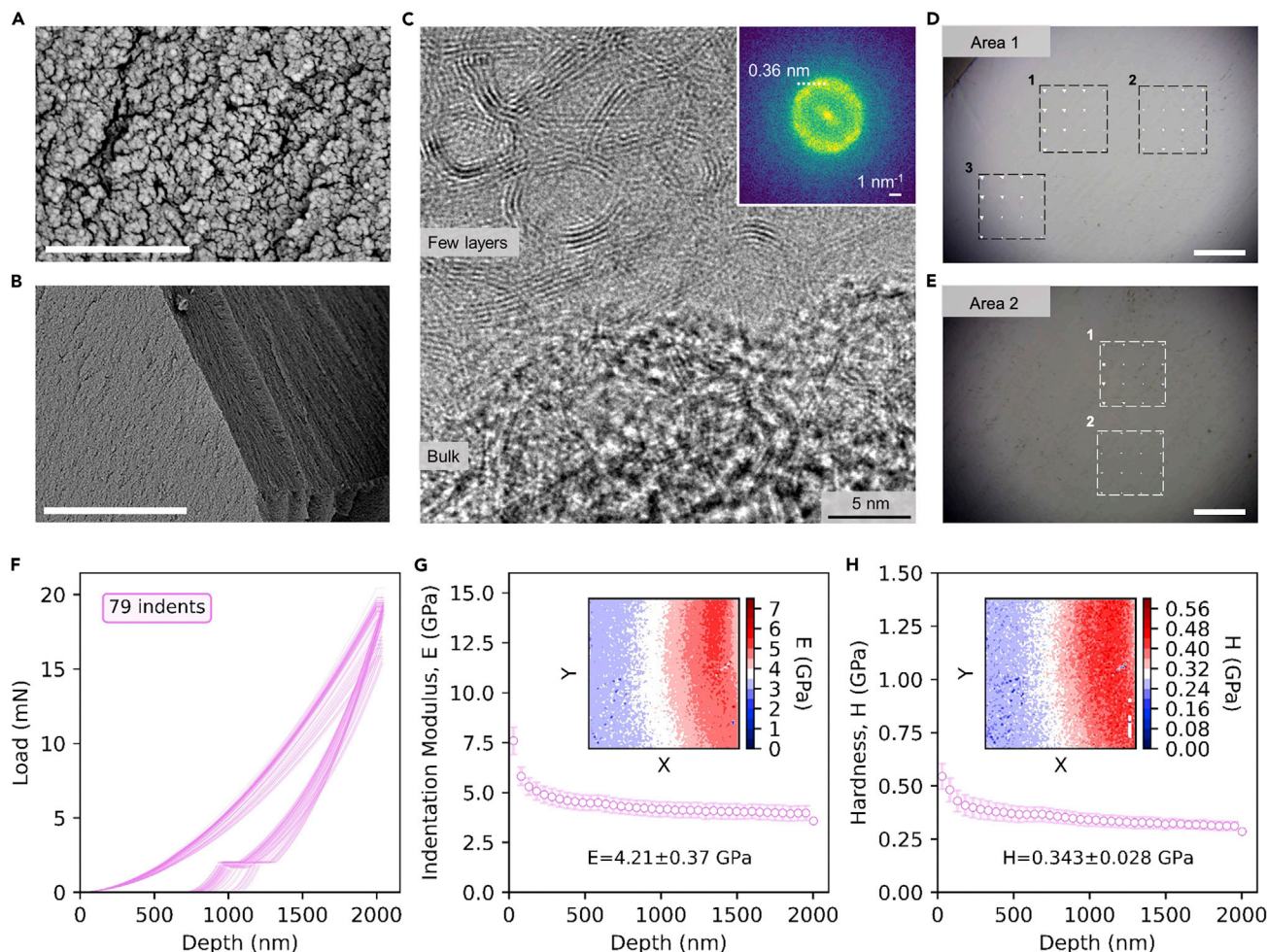


**Figure 4. SEM images, TEM images, and nanoindentation studies of the methanol-activated 1.000 (v/v) TPB-DMTP-COF monolith show the crystalline-to-turbostratic-disordering mechanisms**

(A and B) SEM images of the TPB-DMTP-COF monolith. Scale bars represent 1  $\mu\text{m}$  (A) and 10  $\mu\text{m}$  (B).

(C) HR-TEM image of the TPB-DMTP-COF monolith showing locally layered structures connected by turbostratically disordered regions where the scale bar is 5 nm. The inset shows a fast Fourier transform (FFT) from a thin area, indicating a broad ring, with the peak corresponding to 0.36.

(D and E) Optical micrograph showing the array of residual indents taken in different areas of the monolith. Scale bars represents 100  $\mu\text{m}$ .

(F) Indentation load versus penetration depth for 79 indents.

(G and H) Indentation modulus versus penetration depth (G) and hardness versus penetration depth (H) averaged over 79 indents; error bars represent standard deviations calculated from 79 measurements. The insets show the NanoBlitz indentation mapping measured in a square region of size 200  $\mu\text{m}$ ; the color bar indicates the indentation modulus (E) in (G) and the hardness (H) in (H) at the different positions (x, y).

could give rise to regions of greater or lesser disruption, resulting in macroscopic domains with slightly differing mechanical properties in the finished pellet. Collectively, these findings both confirm the presence of disrupted crystallites in non-porous monoliths and suggest that a turbostratic disordering mechanism is responsible for such observable losses in porosity.

After establishing post-processing conditions capable of explicitly avoiding crystallite damage, we then used a combination of mercury porosimetry and small-angle X-ray scattering (SAXS) to gain insights into the structure of monolith free-volume elements across the mesoscale. Pore-size distributions derived from mercury intrusion curves for a  $\text{scCO}_2$ -activated 1.000 acetonitrile monolith revealed the presence of sharp mesoporosity at 18.7 nm attributable to narrow and regular interparticle



free-volume elements (Figure 3A, inset). Broader macroporosity centered at a pore width of around  $3\ \mu\text{m}$  was also observed. By contrast, a non-monolithic powder control prepared via the method of Xu et al. (BET area of  $1,985\ \text{m}^2\ \text{g}^{-1}$ )<sup>14</sup> exhibited no regular meso- or macroporosity. Analysis of the respective mercury areas for accessible pore widths down to  $3.9\ \text{nm}$  (above that of the intrinsic framework, i.e.,  $2.5\ \text{nm}$ ) further showed an area of  $504\ \text{m}^2\ \text{g}^{-1}$  for the monolith and  $196\ \text{m}^2\ \text{g}^{-1}$  for the powder. These results are comparable to those for classical mesoporous templated silicas and carbons<sup>30,31</sup> and are consistent with those derived from SAXS (Figure 3D and supplemental information section S7). The  $\text{scCO}_2$ -processed monolith was well fit by a spheroidal particle model with two log-normalized-distribution models with mean diameters of  $25.8\ \text{nm}$  ( $\sigma = 0.4$ ) and  $99.8\ \text{nm}$  ( $\sigma = 0.2$ ), indicating the presence of mesoporous interparticle free-volume elements and providing evidence for additional macroporosity. By contrast, the non-monolithic powder control was found to possess an interparticle size distribution beyond the  $0.5\text{--}100\ \text{nm}$  range and, consequently, could not be fitted. These results suggest that COF processing into monoliths can not only be used to avoid pore collapse but also provide additional mesoporosity (inaccessible from powders) that can be used for tuning final uptake performance characteristics—potentially beyond those of purely crystalline systems.

To examine the impact of crystallite disordering on mesoporous free-volume elements, we also analyzed a  $\text{scCO}_2$ -processed monolith activated at an accelerated depressurization rate of  $8\ \text{bar h}^{-1}$  (BET area of  $1,439\ \text{m}^2\ \text{g}^{-1}$ ) by using SAXS (Figure S4). The sample was fit by three spheroidal size-distribution models exhibiting mean diameters of  $14.7\ \text{nm}$  ( $\sigma = 0.3$ ),  $21.1\ \text{nm}$  ( $\sigma = 0.6$ ), and  $98.5\ \text{nm}$  ( $\sigma = 0.1$ ). The emergence of a third, narrow free-volume element along with an overall shift in mesopore distribution to smaller values suggests that disruption of crystallites is concomitant with a reduction in interparticle free volume. Because this reduction in interparticle pore size can be controlled by the  $\text{scCO}_2$  pressure release rate, future opportunities exist for top-down control over monolith microstructure and gas-adsorption properties.

To assess the extent to which COF monoliths can be used as industrial pellets, we carried out nanoindentation studies, from which we derived mechanical indentation moduli and hardness values. For a  $3\ \text{bar h}^{-1}$   $\text{scCO}_2$ -activated  $1.000\ (\text{v/v})$  pellet, we obtained an indentation modulus of  $3.71 \pm 0.20\ \text{GPa}$  and a hardness of  $0.18 \pm 0.02\ \text{GPa}$  (Figures 3B and 3E). These values are significantly higher than those previously obtained for COF aerogel pellets<sup>26</sup> and slightly above those known for high-molecular-weight polyethylene.<sup>32</sup> A full comparison of the mechanical properties of the COF monolith and those of other COF bodies reported in the literature is included in Table S6. These results suggest mechanical robustness and potential industrial suitability, possibly as a result of weak, non-crystalline-layer interfaces between COF crystallites, which serve to dissipate stress.<sup>33,34</sup> By contrast, powder controls crumbled readily and could not be mounted in the instrument to yield reliable results. Further densification of monoliths with the use of higher-surface-tension activation solvents yielded slight increases in both indentation modulus and hardness. For a methanol-activated  $1.000\ (\text{v/v})$  monolith, where pore collapse is complete, the indentation modulus and hardness values were  $4.21 \pm 0.37$  and  $0.34 \pm 0.03\ \text{GPa}$ , respectively (Figures 4D–4H). However, because these values represent modest improvements over the fully porous analog, potential design trade-offs between mechanical properties and porosity are likely to favor porous monoliths. Collectively, the combination of mechanical robustness, high bulk densities, high surface areas, and regular hierarchical mesopores is unique among COF-shaped

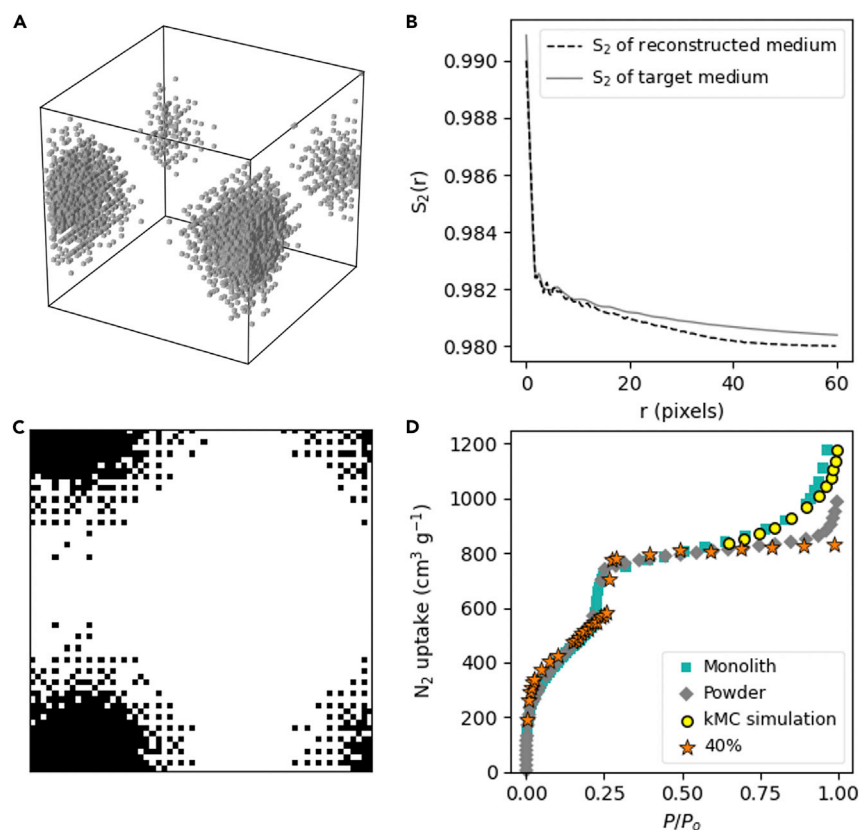


**Figure 5. Lattice-gas model reconstruction and molecular simulations**

(A) Reconstructed 3D realization of the TPB-DMTP-COF monolith defined on a bcc lattice with periodic boundaries; gray (white) voxels represent the solid (void) phase.  
 (B) Comparison of  $S_2(r)$  functions of target and reconstructed medium. The  $S_2(r)$  function of the TPB-DMTP-COF monolith (target medium) is shown in gray, and the  $S_2(r)$  function of the reconstructed medium is shown in black (dashed line).  
 (C) A 2D slice of the 3D realization showing all the possible sites occupied by the solid (black) and void (white) phases. The size of the system is  $60 \times 60 \times 60$  pixels for the 3D realization and  $60 \times 60$  pixels for the 2D slice.  
 (D) Comparison of experimental adsorption isotherms and simulated adsorption isotherms of  $N_2$  at 77 K. The experimental adsorption isotherms are represented by turquoise squares for the  $3 \text{ bar h}^{-1}$   $\text{scCO}_2$ -activated 1.000 (v/v) monolith and by gray diamonds for the powder. Yellow circles correspond to data points obtained from kMC simulations within the lattice-gas model. Orange stars correspond to data points obtained from GCMC simulations taking into consideration a 40% slip between layers.

bodies demonstrated to date. This is illustrated in Figure 3F and Table S6, in which the  $3 \text{ bar h}^{-1}$   $\text{scCO}_2$ -activated 1.000 (v/v) monolith is compared with other COF bodies (including those featuring additives and binders) on the basis of density, BET area, and mechanical figures of merit.

### Molecular simulations and lattice-gas model

To accurately capture the adsorption characteristics of TPB-DMTP-COF *in silico*, we carried out grand canonical Monte Carlo (GCMC) simulations on TPB-DMTP-COF crystalline fragments exhibiting varying degrees of interlayer slip (supplemental information section S2). Starting from perfect AA stacking (0% slip), one of two sequential layers of the COF was gradually shifted until perfect AB stacking was achieved (100% slip). Using cells derived from 0%, 25%, 40%, 50%, 75%, and 100% slipped starting structures (Figure S1), we then used GCMC simulations to

generate predicted nitrogen isotherms at 77 K. Upon comparison of the respective low-pressure regions and mesoporous steps of the experimental adsorption isotherms to those derived from theory, a 40% slipped structure was found to provide the best agreement with experiment, giving almost identical low-pressure adsorption characteristics up to the mesoporous step (Figure 5D). Above the mesoporous step, however, whereas experimental isotherms for TPB-DMTP-COF powders maintained a reasonable agreement with those calculated from the 40% slipped structure until saturation, substantial deviations from theory were observed for experimental isotherms derived from TPB-DMTP-COF monoliths as a result of interparticle mesoporosity. Given that these deviations ultimately push total nitrogen uptake within the monolith above levels expected for purely crystalline systems, the ability to accurately capture such deviations computationally is critical in evaluating and subsequently tuning final gas-uptake characteristics for a desired target application.

To model contributions to total gas uptake arising from interparticle mesopores, we moved to a lattice-gas model of the TPB-DMTP-COF monolith (supplemental information section S4). Lattice-gas models have been extensively used in the past for studying the nature of sorption hysteresis for fluids in confined interconnected void spaces of porous glasses.<sup>35–37</sup> We numerically reconstructed the structural model of the monolith (Figure 5B) used in the lattice-gas model from the SAXS data for the TPB-DMTP-COF monolith by means of generating a two-point correlation function  $S_2(r)$  and using it in the reconstruction algorithm. A 3D reconstructed structure and its 2D slice used in the lattice-gas model for the TPB-DMTP-COF monolith activated by  $\text{scCO}_2$  are shown in Figures 5A and 5C, respectively. To model the trajectory of the system in the grand canonical ensemble, we subsequently employed kinetic Monte Carlo (kMC) simulations from which nitrogen adsorption isotherms at 77 K could be obtained. The numerically generated isotherms show an excellent agreement with experimental data for the TPB-DMTP-COF monolith within the high-pressure region of the adsorption isotherms, providing complementary data to the GCMC-calculated isotherms and demonstrating the applicability of lattice-gas models in capturing the interparticle mesoporosity of COF monoliths. Collectively, these results suggest that the hierarchical porosity of COF monoliths can be accurately described computationally across the micro- and mesoporous ranges, enabling robust future predictions of adsorption characteristics.

### Gas-adsorption characteristics of TPB-DMTP-COF monoliths

To demonstrate the utility of monolithic processing of COFs in gas-storage applications, we performed pure-component adsorption studies on TPB-DMTP-COF powders and monoliths. Low-pressure isotherms collected at 298 K revealed good  $\text{CO}_2$  (Figures 6A and 6D) uptake for both powders and monoliths with modest to low  $\text{CH}_4$  (Figure 6A) and  $\text{N}_2$  (Figure 6D) uptake, respectively, for both systems. However, up to pressures of 1 bar, although higher  $\text{CO}_2$  uptake was obtained for monoliths than for powders, lower uptake for both  $\text{CH}_4$  and  $\text{N}_2$  was obtained for monoliths than for powders. These results suggest that the presence of interparticle mesopores in monoliths can be used not only for improving final storage capacities for a single component but also for favorably or unfavorably influencing final uptake characteristics of various components within a mixed feed.

To examine these characteristics within the context of chemical separations, we evaluated adsorption selectivities for industrially relevant compositions of  $\text{CO}_2$ ,  $\text{CH}_4$ , and  $\text{N}_2$  mixtures. From pure-component adsorption isotherms and using the ideal absorbed solution theory (IAST), we calculated selectivities for 15%  $\text{CO}_2$ /85%  $\text{N}_2$  (Figure 6E) and 50%  $\text{CO}_2$ /50%  $\text{CH}_4$  (Figure 6B) (v/v) mixtures (supplemental

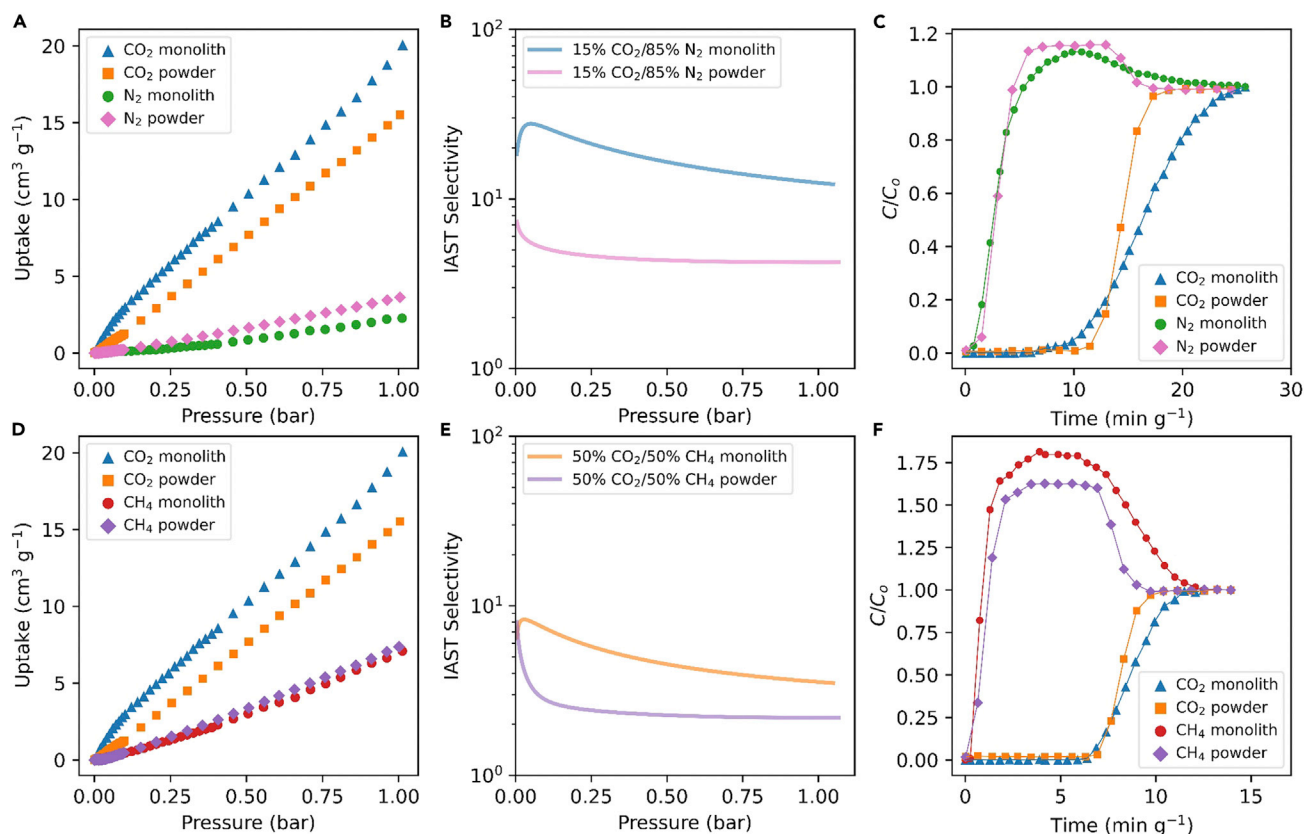


**Figure 6. Low-pressure adsorption isotherms, IAST selectivity, and breakthrough studies of TPB-DMTP-COF ( $3 \text{ bar h}^{-1} \text{ scCO}_2$ -activated 1.000 [v/v] monolith and powder control)**

(A) Low-pressure adsorption isotherms of  $\text{CO}_2$  and  $\text{N}_2$  at 298 K in TPB-DMTP-COF monolith (blue triangles for  $\text{CO}_2$  and green circles for  $\text{N}_2$ ) and powder (orange squares for  $\text{CO}_2$  and pink diamonds for  $\text{N}_2$ ).  
 (B) IAST selectivity as a function of pressure for a 15%  $\text{CO}_2$ /85%  $\text{N}_2$  gas mixture for TPB-DMTP-COF monolith (blue) and powder (pink).  
 (C) Breakthrough studies for a 15%  $\text{CO}_2$ /85%  $\text{N}_2$  gas mixture for TPB-DMTP-COF monolith ( $\text{CO}_2$ , blue triangles;  $\text{N}_2$ , green circles) and powder ( $\text{CO}_2$ , orange squares;  $\text{N}_2$ , pink diamonds) at 298 K.  
 (D) Low-pressure adsorption isotherms of  $\text{CO}_2$  and  $\text{CH}_4$  at 298 K in TPB-DMTP-COF monolith (blue triangles for  $\text{CO}_2$  and red circles for  $\text{CH}_4$ ) and powder (orange squares for  $\text{CO}_2$  and purple diamonds for  $\text{CH}_4$ ).  
 (E) IAST selectivity as a function of pressure for a 50%  $\text{CO}_2$ /50%  $\text{CH}_4$  gas mixture for TPB-DMTP-COF monolith (orange) and powder (purple).  
 (F) Breakthrough studies for a 50%  $\text{CO}_2$ /50%  $\text{CH}_4$  gas mixture for TPB-DMTP-COF monolith ( $\text{CO}_2$ , blue triangles;  $\text{CH}_4$ , red circles) and powder ( $\text{CO}_2$ , orange squares;  $\text{CH}_4$ , purple diamonds) at 298 K.

information section S8). At low pressures, the selectivity for  $\text{CO}_2$  relative to other components was substantially improved, providing evidence that monolithic COF structuring can be used to provide separation enhancements relative to unstructured COF powders. To confirm this, we performed dynamic breakthrough studies on TPB-DMTP-COF monoliths and powders by using mixed-gas feeds. For the 15%  $\text{CO}_2$ /85%  $\text{N}_2$  mixture (Figure 6F), although comparable separations were achieved for the monolith and powder (and some additional evidence for axial dispersion was observed), the total  $\text{CO}_2$  uptake was found to be 13.4% higher for the monolith. For the 50%  $\text{CO}_2$ /50%  $\text{CH}_4$  mixture (Figure 6C), a markedly sharper separation for the monolith than for the powder was observed, and an additional improvement in  $\text{CO}_2$  capacity of 8.6% was achieved. Tables S6 and S7 compare these results against those for similar separations reported in the literature. Collectively, these results not only demonstrate the utility of monolithic processing for adsorbent-based chemical storage and separation but also afford additional



degrees of freedom through which the properties of COFs can be systematically designed and tuned.

## Conclusions

Using a simple and general processing workflow, we introduce methods for the preparation of hierarchically porous COF monoliths without the need for additional materials or processing components. We show that such processing methods are compatible with mechanically weak materials and further afford degrees of design freedom in the control of both extrinsic and intrinsic porosities. These characteristics endow monolithic COFs with properties that are distinct from both powder and single-crystal analogs, which we accurately capture *in silico* by using a lattice-gas model. We envision that such computational approaches can be used in the future to predict gas-uptake properties for broad classes of monolithic mesoporous materials. The extrinsic porosity present in COF monoliths can further be leveraged for simultaneously increasing and decreasing the final uptake capacities for various gas constituents relative to powder benchmarks, which we make use of in demonstrating improved separation performance for industrially relevant gas compositions. We believe that this study not only opens up new possibilities for the practical applicability of COFs but also provides a pathway forward for tuning sorbent-analyte interactions where changes to the underlying framework chemistry might not be possible or synthetically accessible.

## EXPERIMENTAL PROCEDURES

### Resource availability

#### Lead contact

Further information and requests for resources should be directed to and will be fulfilled by the lead contact, David Fairen-Jimenez ([df334@cam.ac.uk](mailto:df334@cam.ac.uk)).

#### Materials availability

The experimental dataset and materials generated and/or analyzed during the current study are available from the lead contact upon reasonable request.

#### Data and code availability

Adsorption information files (AIFs), Materials Studio scripts, mechanical-property data, RASPA input files, SAXS data, and crystallographic information files (CIFs) are included in the [supplemental information](#). Any raw data and code used for analysis not included in the [supplemental information](#) are available from the lead contact upon reasonable request.

## Materials

Scandium(III)trifluoromethanesulfonate (98%) was purchased from Alfa Aesar; 1,3,5-tris(4-aminophenyl)benzene (93%) was purchased from TCI; 2,5-dimethoxybenzene-1,4-dicarboxaldehyde (97%) was purchased from Sigma-Aldrich; and methanol (99.9%), acetonitrile (99.9+%), 1,3,5-trimethylbenzene (99%), and 1,4-dioxane (99.5%) were purchased from Acros Organics. All chemicals were used as received without further purification.

## Synthesis of TPB-DMTP-COFs

### Monoliths

To a 50 mL centrifuge tube were added 1,3,5-tris(4-aminophenyl)benzene (140.60 mg, 400  $\mu$ mol) and 2,5-dimethoxybenzene-1,4-dicarboxaldehyde (29.13 mg, 150  $\mu$ mol). Solvent (16 mL) was then added, and the mixture was sonicated briefly to a homogeneous suspension. Scandium(III) trifluoromethanesulfonate<sup>38</sup> (12 mg, 24  $\mu$ mol) was

added, the tube was sealed, and the mixture was sonicated again for approximately 20 s. The mixture was then left to react for 30 min undisturbed. The sample was collected by centrifugation for 50 min, washed with three portions of solvent (40 mL each) and an additional portion of methanol (40 mL), and was solvent exchanged in methanol (40 mL) at 50°C for 48 h; the solvent was then replaced after 24 h. The solvent was then decanted, and the sample was washed with methanol (40 mL) and left to dry at 20°C for a further 24 h or dried with  $\text{scCO}_2$ . The sample was activated overnight at 120°C under vacuum prior to characterization.

#### Powders

The TPB-DMTP-COF powder controls were synthesized according to a previously reported procedure.<sup>14</sup>

### Characterization of TPB-DMTP-COF

#### Total scattering data

Total scattering data were collected at beamline 11-ID-B of the Advanced Photon Source of the Argonne National Laboratory.<sup>39</sup> Monoliths were segmented into regions (rim, top, and bottom; Figure S6) and lightly ground before being loaded into 1.1 mm (outer diameter) Kapton capillaries. High-energy X-ray scattering data were recorded with a Perkin Elmer amorphous silicon-based area detector with an X-ray wavelength of 0.2115 Å at a sample-to-detector distance of ca. 180 mm—experimental geometry was calibrated with a  $\text{CeO}_2$  diffraction standard. The images were calibrated and reduced to 1D diffraction data within GSAS-II.<sup>40</sup> The X-ray scattering measured for an empty Kapton capillary was used as the sample background. The data were background corrected in xPDFsuite,<sup>41</sup> and  $G(r)$  was calculated with data in the range  $0.1 \text{ Å}^{-1} \leq Q \leq 23.1 \text{ Å}^{-1}$ . Full details and discussion on the total scattering data are included in supplemental information section S6. SEM images were acquired by an FEI XL30 FEGSEM with an accelerating voltage of 5 kV. Samples were sputter coated with gold. TEM was carried out on a FEI Tecnai F20 TEM operated at 200 kV, and images were acquired with a Gatan OneView camera.

#### Helium pycnometry

Helium pycnometry was obtained with an AccuPyc 1330 Pycnometer from Micromeritics. This technique was used to estimate the particle density and the volume of both powders and monoliths by measuring the pressure change of helium in a calibrated volume. Each volume was recorded as an average value of six consecutive runs. Prior to the analysis, all samples were activated overnight at 120°C (vacuum) before the mass was measured.

#### Mercury porosimetry

Mercury porosimetry was obtained up to a final pressure of 2,000 bar with an AutoPore IV 9500 instrument from Micromeritics. This technique was used to estimate the particle density of both powders and monoliths at atmospheric pressure. Prior to the analysis, all samples were activated overnight at 120°C (vacuum) before the mass was measured and then degassed *in situ* thoroughly before the mercury porosimetry.

#### Critical point dryer- $\text{CO}_2$ procedure

A SPI-DRY critical point dryer (jumbo size) modified with a manometer at the chamber was used to dry and activate the COF monoliths. First, the sample was transferred into a dialysis membrane (Spectra/P.1 MWCO 6–8 kD) and sealed. Then, the membrane was introduced into the critical point drying equipment. Then, it was immersed in

subcritical (l) CO<sub>2</sub> at 283 K and 50 bar for half an hour. Then, the exchanged methanol was removed through a purge valve and then flushed with fresh (l) CO<sub>2</sub>. This process was repeated three times. Subsequently, the temperature was raised 5 K min<sup>-1</sup> up to 313 K to exceed the scCO<sub>2</sub> point. Finally, under constant temperature (313 K), the chamber was vented at 8 or 3 bar h<sup>-1</sup> to atmospheric pressure.

#### Gas-adsorption measurements

Ultra-high-purity-grade CH<sub>4</sub>, N<sub>2</sub>, and CO<sub>2</sub> were used for gas-sorption experiments. Adsorption experiments (up to 1 bar) for different pure gases were performed on a Micromeritics 3 Flex surface-area and pore-size analyzer. About 200 mg of activated sample was used for the measurements. A temperature-controlled bath was used to maintain a constant temperature in the bath throughout the duration of the experiment. Samples were degassed on a Micromeritics PrepStation instrument prior to the analysis.

#### Dynamic mixed-gas breakthrough studies

In a typical experiment, ca. 0.3 g of pre-activated sample was placed in a quartz tube (Ø = 8 mm) to form a fixed bed held in place by quartz wool. For monolithic samples, we broke and sieved individual monoliths to reduce the particle diameter to ca. 2 mm to ensure good packing within the sample tube. We heated each sample to 353 K under a dry helium flow to remove atmospheric contaminants. Upon cooling, the chosen gas mixture was passed over the packed bed with a total flow rate of 2 cm<sup>3</sup> min<sup>-1</sup> at 298 K. The outlet gas concentration was continuously monitored with an Agilent 5975 MSD mass spectrometer. Upon complete breakthrough and saturation of the packed bed adsorbent, the gas mixture was switched off, and dry helium was flowed over the solid. Heating was switched on, and samples were heated to 353 K to aid regeneration.

To calculate the CO<sub>2</sub> uptake, we initially passed the gas mixture through an empty reactor containing quartz wool at a flow rate of 2 cm<sup>3</sup> min<sup>-1</sup> as a blank reference. The gas flow was constantly monitored by the mass spectrometer. We integrated the CO<sub>2</sub> curve to calculate the area of the curve ( $A_{\text{Ref}}$ ). Upon completion of a CO<sub>2</sub> breakthrough experiment with an adsorbent, we also integrated the area of the CO<sub>2</sub> adsorption curve ( $A_{\text{Exp}}$ ). To calculate the total amount of CO<sub>2</sub> adsorbed, we used the following equation:

$$\text{total CO}_2 \text{ uptake} = (A_{\text{Ref}} - A_{\text{Exp}}) \times \text{CO}_2 \text{ flow (cm}^3 \text{ min}^{-1}\text{)}$$

#### Molecular simulations

The adsorption isotherms of N<sub>2</sub> were simulated by the GCMC method as implemented in the RASPA simulation package.<sup>42</sup> The geometric properties were calculated with Poreblazer.<sup>43,44</sup> A more detailed description of the methodology and model parameters is given in [supplemental information section S2](#).

#### Lattice-gas model

First, the collected SAXS data were converted into a two-point correlation function  $S_2(r)$  (defined as the probability of two points separated by distance  $r$ , belonging to the pore space of the medium), which was then used as a benchmark for creating a 3D reconstruction of the TPB-DMTP-COF monolith. In order to model the trajectory of the system in the grand canonical ensemble and to obtain the adsorption isotherms, we employed kMC simulations. A more detailed description of the reconstruction procedure and the kMC simulations is given in [supplemental information section S4](#).

### Calculation of mechanical properties

Mechanical properties for the COFs present in the CURATED COF database were calculated with classical molecular mechanics via the “constant strain approach” as implemented in the Forcite module of Materials Studio. Some CURATED structures for which either the mechanical or the geometric property calculation failed were excluded. The mechanical properties calculated included the shear modulus, bulk modulus, and Young’s modulus. A more detailed description of the methodology used is given in [supplemental information section S5](#).

### Calculation of BET area

BET areas were calculated with a computational tool called BETSI, which makes an unambiguous calculation of the possible BET area. More details about BETSI can be found in [supplemental information section S9](#).

### Nanoindentation tests

Nanoindentation tests were carried out for measuring the mechanical properties, namely indentation modulus<sup>45</sup> (E) and hardness (H) of the 3 bar h<sup>−1</sup> scCO<sub>2</sub>-activated 1.000 (v/v) TPB-DMTP-COF monolith, the methanol-activated 1.000 (v/v) TPB-DMTP-COF monolith, and the TPB-DMTP-COF powder. In order to perform the tests, we cold mounted the sample in epoxy and polished it with sandpapers and diamond suspension (up to a 0.1 μm grain size). This was not possible for the TPB-DMTP-COF powder because it crumbled into small pieces. All tests were carried out with a KLA iMicro nanoindenter equipped with a 50 mN force actuator. A Berkovich diamond indenter tip was used. Continuous stiffness measurements (CSMs) were performed, allowing measurement of E and H as a function of the indentation depth. The maximum indentation depth was set to 2,000 nm for all tests. Average values of E and H were computed in the range of 500–2,000 nm. For the methanol-activated 1.000 (v/v) TPB-DMTP-COF monolith, the NanoBlitz 3D mode was used to generate indentation maps of nanomechanical properties. Three maps in three different areas of the sample were taken.

## SUPPLEMENTAL INFORMATION

Supplemental information can be found online at <https://doi.org/10.1016/j.chempr.2022.07.013>.

## ACKNOWLEDGMENTS

M.E.C. acknowledges the support of the His Royal Highness the Prince of Wales Commonwealth Scholarship and the Trinity Henry Barlow Scholarship (honorary). N.R. acknowledges the support of the Cambridge International Scholarship and the Trinity Henry Barlow Scholarship (honorary). The X-ray total scattering measurements and multivariate analysis were supported as part of GENESIS: A Next-Generation Synthesis Center, an Energy Frontier Research Center funded by the US Department of Energy (DOE) Office of Science Basic Energy Sciences Program under award number DE-SC0019212. This research used beamline 11-ID-B of the Advanced Photon Source, a US DOE Office of Science User Facility operated for the DOE Office of Science by Argonne National Laboratory under contract no. DE-AC02-06CH11357. D.F.-J. thanks the Royal Society for a university research fellowship. We thank the European Research Council (ERC) under the European Union’s Horizon 2020 Research and Innovation Programme (NanoMOFdeli, ERC-2016-COG 726380) and Innovate UK (104384). J.S.-A. acknowledges financial support from MINECO (PID2019-108453GB-C21). J.-C.T. and M.T. appreciate the ERC Consolidator Grant (PROMOFS 771575) for supporting the research. J.A.M.-I.



and F.Z. acknowledge support from the Ministerio de Ciencia e Innovación (PID2019-106268GB-C32).

## AUTHOR CONTRIBUTIONS

M.E.C. and D.F.-J. designed the research. M.E.C. synthesized and characterized the materials. M.E.C., D.G.M., and C.C. performed the N<sub>2</sub> gas adsorption at 77 K. D.G.M. and C.C. performed the N<sub>2</sub>, CO<sub>2</sub>, and CH<sub>4</sub> gas adsorption at 298 K. D.G.M. conducted the dynamic mixed-gas breakthrough analysis with supervision from T.C. N.P.M.C. carried out the SAXS and WAXS data collection. D.O.N. performed the SAXS and WAXS data analysis. D.O.N. and K.W.C. collected and analyzed the PDF-XRD data. G.D. carried out the TEM analysis. M.E.C. carried out the SEM analysis. N.R. and R.C. carried out the lattice-gas modeling under the supervision of S.T. N.R. carried out the molecular simulations and mechanical property screens. J.A.M.-I. performed the scCO<sub>2</sub> drying and activation under the supervision of F.Z. J.S.-A. carried out the mercury porosimetry. M.T. performed the nanoindentation experiments and data analysis under the supervision of J.-C.T. M.E.C., N.R., and D.F.-J. wrote the manuscript with contributions from all authors.

## DECLARATION OF INTERESTS

M.E.C. and D.F.-J. are inventors on international patent application no. WO2021052969A1, which covers COF monoliths, as well as aspects of their use. D.F.-J. has a financial interest in the start-up company Immaterial Labs, which is seeking to commercialize MOFs.

Received: January 4, 2022

Revised: May 16, 2022

Accepted: July 14, 2022

Published: August 23, 2022

## REFERENCES

- Sholl, D.S., and Lively, R.P. (2016). Seven chemical separations to change the world. *Nature* 532, 435–437.
- Schoedel, A., Ji, Z., and Yaghi, O.M. (2016). The role of metal–organic frameworks in a carbon-neutral energy cycle. *Nat. Energy* 1, 16034.
- Diercks, C.S., and Yaghi, O.M. (2017). The atom, the molecule, and the covalent organic framework. *Science* 355, eaal1585.
- Slater, A.G., and Cooper, A.I. (2015). Porous materials. Function-led design of new porous materials. *Science* 348, aaa8075.
- Huang, N., Wang, P., and Jiang, D. (2016). Covalent organic frameworks: A materials platform for structural and functional designs. *Nat. Rev. Mater.* 1, 16068.
- Sun, J., Iakunkov, A., Baburin, I.A., Joseph, B., Palermo, V., and Talyzin, A.V. (2020). Covalent organic framework (COF-1) under high pressure. *Angew. Chem. Int. Ed.* 59, 1087–1092.
- Du, Y., Calabro, D., Wooler, B., Li, Q., Cundy, S., Kamakoti, P., Colmyer, D., Mao, K., and Ravikovitch, P. (2014). Kinetic and mechanistic study of COF-1 phase change from a staggered to eclipsed model upon partial removal of mesitylene. *J. Phys. Chem. C* 118, 399–407.
- Sick, T., Rotter, J.M., Reuter, S., Kandambeth, S., Bach, N.N., Döblinger, M., Merz, J., Clark, T., Marder, T.B., Bein, T., and Medina, D.D. (2019). Switching on and off interlayer correlations and porosity in 2D covalent organic frameworks. *J. Am. Chem. Soc.* 141, 12570–12581.
- Feriante, C.H., Jhulki, S., Evans, A.M., Dasari, R.R., Slicker, K., Dichtel, W.R., and Marder, S.R. (2020). Rapid synthesis of high surface area imine-linked 2D covalent organic frameworks by avoiding pore collapse during isolation. *Adv. Mater.* 32, e1905776.
- Zhu, D., and Verdusco, R. (2020). Ultralow surface tension solvents enable facile COF activation with reduced pore collapse. *ACS Appl. Mater. Interfaces* 12, 33121–33127.
- Zhou, W., Wu, H., and Yildirim, T. (2010). Structural stability and elastic properties of prototypical covalent organic frameworks. *Chem. Phys. Lett.* 499, 103–107.
- Uribe-Romo, F.J., Vazquez-Molina, D., and Harper, J.K. (2019). Mechanically shaped 2-dimensional covalent organic frameworks. US patent no. WO2018013682A1. published September 9, 2019.
- Moghadam, P.Z., Rogge, S.M.J., Li, A., Chow, C.-M., Wieme, J., Moharrami, N., Aragones-Anglada, M., Conduit, G., Gomez-Gualdrón, D.A., Van Speybroeck, V., and Fairen-Jimenez, D. (2019). Structure-mechanical stability relations of metal-organic frameworks via machine learning. *Matter* 1, 219–234.
- Xu, H., Gao, J., and Jiang, D. (2015). Stable, crystalline, porous, covalent organic frameworks as a platform for chiral organocatalysts. *Nat. Chem.* 7, 905–912.
- Ongari, D., Yakutovich, A.V., Talirz, L., and Smit, B. (2019). Building a consistent and reproducible database for adsorption evaluation in covalent–organic frameworks. *ACS Cent. Sci.* 5, 1663–1675.
- Howarth, A.J., Liu, Y., Li, P., Li, Z., Wang, T.C., Hupp, J.T., and Farha, O.K. (2016). Chemical, thermal and mechanical stabilities of metal-organic frameworks. *Nat. Rev. Mater.* 1, 15018.
- Tian, T., Zeng, Z.X., Vulpe, D., Casco, M.E., Divitini, G., Midgley, P.A., Silvestre-Albero, J., Tan, J.C., Moghadam, P.Z., and Fairen-Jimenez, D. (2018). A sol-gel monolithic metal-organic framework with enhanced methane uptake. *Nat. Mater.* 17, 174–179.

18. Connolly, B.M., Aragonés-Anglada, M., Gandara-Loe, J., Danaf, N.A., Lamb, D.C., Mehta, J.P., Vulpe, D., Wuttke, S., Silvestre-Albero, J., Moghadam, P.Z., et al. (2019). Tuning porosity in macroscopic monolithic metal-organic frameworks for exceptional natural gas storage. *Nat. Commun.* **10**, 2345.
19. Connolly, B.M., Madden, D.G., Wheatley, A.E.H., and Fairen-Jimenez, D. (2020). Shaping the future of fuel: Monolithic metal-organic frameworks for high-density gas storage. *J. Am. Chem. Soc.* **142**, 8541–8549.
20. Chapman, K.W., Halder, G.J., and Chupas, P.J. (2009). Pressure-induced amorphization and porosity modification in a metal-organic framework. *J. Am. Chem. Soc.* **131**, 17546–17547.
21. Kandambeth, S., Dey, K., and Banerjee, R. (2019). Covalent organic frameworks: Chemistry beyond the structure. *J. Am. Chem. Soc.* **141**, 1807–1822.
22. Osterrieth, J.W.M., Rampersad, J., Madden, D., Rampal, N., Skoric, L., Connolly, B., Allendorf, M.D., Stavila, V., Snider, J.L., Ameloot, R., et al. (2022). How reproducible are surface areas calculated from the BET equation? *Adv. Mater.* **34**, e2201502.
23. Song, C., Wang, P., and Makse, H.A. (2008). A phase diagram for jammed matter. *Nature* **453**, 629–632.
24. Ma, Q., Zeng, L., Liu, X.Y., Zhuang, Q.X., and Qian, J. (2022). A simple and efficient method for preparing covalent organic framework aerogels with ultra-light and super-elastic. *Micropor. Mesopor. Mater.* **331**, 111623.
25. Zhu, D., Zhu, Y., Yan, Q., Barnes, M., Liu, F., Yu, P., Tseng, C.-P., Tjahjono, N., Huang, P.-C., Rahman, M.M., et al. (2021). Pure crystalline covalent organic framework aerogels. *Chem. Mater.* **33**, 4216–4224.
26. Martín-Illán, J.Á., Rodríguez-San-Miguel, D., Castillo, O., Beobide, G., Perez-Carvajal, J., Imaz, I., Maspoch, D., and Zamora, F. (2021). Macroscopic ultralight aerogel monoliths of imine-based covalent organic frameworks. *Angew. Chem. Int. Ed.* **60**, 13969–13977.
27. Wang, S., Zhang, C., Zhang, Z.Y., Yang, Y.H., Li, Q.L., Wang, W.J., Li, B.G., and Liu, P.W. (2021). Asymmetrical exchange of monomers for constructing hollow nanoparticles and antifragile monoliths. *Matter* **4**, 618–634.
28. Li, C.X., Yang, J., Pachfule, P., Li, S., Ye, M.Y., Schmidt, J., and Thomas, A. (2020). Ultralight covalent organic framework/graphene aerogels with hierarchical porosity. *Nat. Commun.* **11**, 4712.
29. Ding, L.G., Yao, B.J., Li, F., Shi, S.C., Huang, N., Yin, H.B., Guan, Q., and Dong, Y.B. (2019). Ionic liquid-decorated COF and its covalent composite aerogel for selective CO<sub>2</sub> adsorption and catalytic conversion. *J. Mater. Chem. A* **7**, 4689–4698.
30. Lee, J., Sohn, K., and Hyeon, T. (2001). Fabrication of novel mesocellular carbon foams with uniform ultralarge mesopores. *J. Am. Chem. Soc.* **123**, 5146–5147.
31. Zhang, F.-A., Lee, D.-K., and Pinnavaia, T.J. (2010). PMMA/mesoporous silica nanocomposites: Effect of framework structure and pore size on thermomechanical properties. *Polym. Chem.* **1**, 107–113.
32. Iqbal, T., Camargo, S.S., Yasin, S., Farooq, U., and Shakeel, A. (2020). Nano-indentation response of ultrahigh molecular weight polyethylene (UHMWPE): a detailed analysis. *Polymers* **12**, 795.
33. Cook, J., and Gordon, J. (1964). A mechanism for the control of crack propagation in all-brittle systems. *Proc. R. Soc. Lond. A* **282**, 508–520.
34. Clegg, W.J., Kendall, K., Alford, N.M., Button, T.W., and Birchall, J.D. (1990). A simple way to make tough ceramics. *Nature* **347**, 455–457.
35. Evans, R. (1990). Fluids adsorbed in narrow pores: Phase equilibria and structure. *J. Phys. Condens. Matter* **2**, 8989–9007.
36. Gelb, L.D., Gubbins, K.E., Radhakrishnan, R., and Sliwinski-Bartkowiak, M. (1999). Phase separation in confined systems. *Rep. Prog. Phys.* **62**, 1573–1659.
37. Kierlik, E., Rosinberg, M.L., Tarjus, G., and Pitard, E. (1998). Mean-spherical approximation for a lattice model of a fluid in a disordered matrix. *Mol. Phys.* **95**, 341–351.
38. Matsumoto, M., Dasari, R.R., Ji, W., Feriante, C.H., Parker, T.C., Marder, S.R., and Dichtel, W.R. (2017). Rapid, low temperature formation of imine-linked covalent organic frameworks catalyzed by metal triflates. *J. Am. Chem. Soc.* **139**, 4999–5002.
39. Chupas, P.J., Chapman, K.W., and Lee, P.L. (2007). Applications of an amorphous silicon-based area detector for high-resolution, high-sensitivity and fast time-resolved pair distribution function measurements. *J. Appl. Crystallogr.* **40**, 463–470.
40. Toby, B.H., and Von Dreele, R.B. (2013). GSAS-II: The genesis of a modern open-source all purpose crystallography software package. *J. Appl. Crystallogr.* **46**, 544–549.
41. Yang, X., Juhas, P., Farrow, C., and Billinge, S. (2014). xPDFsuite: An end-to-end software solution for high throughput pair distribution function transformation, visualization and analysis. Preprint at arXiv. <https://doi.org/10.48550/arXiv.1402.3163>.
42. Dubbeldam, D., Calero, S., Ellis, D.E., and Snurr, R.Q. (2016). RASPA: Molecular simulation software for adsorption and diffusion in flexible nanoporous materials. *Simulat* **42**, 81–101.
43. Sarkisov, L., and Harrison, A. (2011). Computational structure characterisation tools in application to ordered and disordered porous materials. *Simulat* **37**, 1248–1257.
44. Sarkisov, L., Bueno-Perez, R., Sutharson, M., and Fairen-Jimenez, D. (2020). Materials informatics with PoreBlazer v4.0 and the CSD MOF database. *Chem. Mater.* **32**, 9849–9867.
45. Tan, J.C., Merrill, C.A., Orton, J.B., and Cheetham, A.K. (2009). Anisotropic mechanical properties of polymorphic hybrid inorganic-organic framework materials with different dimensionalities. *Acta Mater.* **57**, 3481–3496.